Journal of Colloid and Interface Science 618 (2022) 270–282

Contents lists available at ScienceDirect

Journal of Colloid and Interface Science

journal homepage: www.elsevier.com/locate/jcis

Acidity-responsive nanocages as robust reactive oxygen species generators with butterfly effects for maximizing oxidative damage and enhancing cancer therapy

Xingru Zhao [a,b], Xingyi Wan [a,b], Tian Huang [a,c], Shuncheng Yao [a,b], Shaobo Wang [a,c], Yiming Ding [a,c], Yunchao Zhao [a,c], Zhou Li [a,b,c], Linlin Li [a,b,c,*]

[a] Beijing Institute of Nanoenergy and Nanosystems, Chinese Academy of Sciences, Beijing 101400, PR China
[b] School of Nanoscience and Technology, University of Chinese Academy of Sciences, Beijing 100049, PR China
[c] Center on Nanoenergy Research, School of physical Science and Technology, Guangxi University, Nanning 530004, PR China

GRAPHICAL ABSTRACT

A pH-responsive core-shell nanocage composed of $CaCO_3$ nanolayer and heterogeneous CoP core ($CaCO_3$@CoP, CCP) is fabricated to amplify the synergy of CDT and calcium overload. The reciprocal interaction and loop feedback between calcium overload and photo-enhanced ROS generation via PTT triggers immune cell death (ICD) process to realize effective immunostimulatory cancer therapy in vivo.

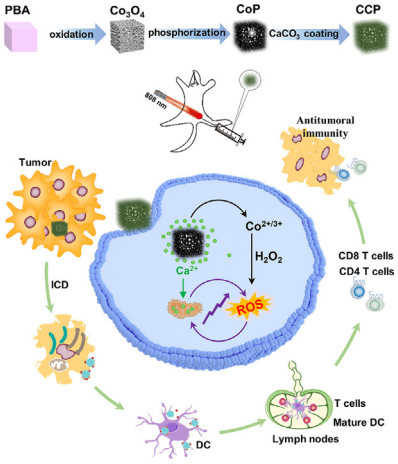

ARTICLE INFO

Article history:
Received 6 January 2022
Revised 18 March 2022
Accepted 19 March 2022
Available online 21 March 2022

Keywords:
Transition metal phosphides
Tumor microenvironment

ABSTRACT

Recently, with the rational design of transition metal-containing nanoagents, chemodynamic therapy (CDT) has been developed and considered a promising method for cancer therapy through Fenton and Fenton-like reaction-induced hydroxyl radical (·OH) generation and cellular oxidative damage. However, it is still a great challenge to realize high reactive oxygen species (ROS) generation and therapeutic efficiency under the strict conditions of the tumor microenvironment (TME). Herein, we design and fabricate a TME-responsive core-shell nanocage composed of a $CaCO_3$ nanolayer and a heterogeneous CoP core ($CaCO_3$@CoP, CCP) with the synergy of CDT and calcium overload to maximize oxidative damage and enhance cancer therapy. The $CaCO_3$ nanoshell is sensitive to pH and can be rapidly degraded upon

* Corresponding author.
E-mail address: lilinlin@binn.cas.cn (L. Li).

https://doi.org/10.1016/j.jcis.2022.03.084

Calcium overload
Chemodynamic therapy
Immune cell death

endocytosis, leading to intracellular Ca^{2+} accumulation, which further triggers the production of mitochondrial ROS. Subsequently, the CoP hollow nanocage with fully exposed Co active sites has high Fenton-like reactive activity to produce ·OH and induce mitochondrial damage. Mitochondrial damage and ROS elevation, in turn, can modulate Ca^{2+} dynamics and augment calcium overload. The reciprocal interaction and loop feedback between calcium overload and photoenhanced ROS generation via photothermal therapy (PTT) can further trigger the immunogenic cell death (ICD) process to activate the maturation of dendritic cells (DCs), activation of cytotoxic and helper T cells, and excretion of proinflammatory cytokines to enhance antitumor immunity in vivo. With the butterfly effect, CCP finally brings forth a greatly enhanced cancer therapeutic outcome in murine models.

1. Introduction

Recently, chemodynamic therapy (CDT) has been proposed as a complementary method for cancer therapy. The method relies on Fenton or Fenton-like reactions of transition metal-containing nanomaterials to produce toxic hydroxyl radicals (·OH), inducing mitochondrial dysfunction, fatal oxidative damage and cancer cell death [1–6]. Since its birth, various CDT nanoagents have been developed, such as transition metals, metallic oxides, metal sulfides, and metal phosphide nanomaterials [7–11]. In this therapeutic strategy, CDT nanoagents are designed to respond to the tumor microenvironment (TME), which is characterized by mild acidity (pH 6.5–7.0) and overproduction of H_2O_2 [12–16]. Unfortunately, despite great efforts, the ROS generation ability and cell killing effect are still not high enough to eliminate tumors via CDT alone [17–18]. The low therapeutic effect of currently developed CDT nanoagents is mainly attributed to the following two reasons. First, those CDT nanoagents often have high reactive activity in strong acid pH 2–5. Nevertheless, the mild acidity of tumors stemming from aerobic glycolysis is one of the main features of the tumor environment, in which the reactive activity of CDT nanoagents is greatly reduced [19]. Second, in tumor cells, multiple redox pathways are tightly interwoven with each other and interdependent to regulate the activity of the cells. The cells might easily escape or recover from oxidative damage with the powerful and upregulated antioxidant defensive system. Together, tackling the two problems from both aspects simultaneously is an appealing therapeutic possibility to induce synthetic lethality and defeat cancer. This outcome is expected to be achieved by simultaneously improving the efficiency of CDT nanoagents and breaking the intracellular redox balance to finally lead to cancer cell death.

Studies have shown that P species are present in many natural enzymes, helping electrons to penetrate from the substrate to the catalytic center. Moreover, the P atoms may share electrons with highly electronegative N, S, O and other atoms to enhance the stability, and ultimately increase the inherent properties of each active site [20–21]. Recently, transition metal phosphides (TMPs) have attracted great interest for photoelectrocatalysis due to their high catalytic activity over wide pH range [22]. TMPs have metalloid properties, an adjustable electronic structure, fast charge transfer, and a wide light absorption range due to the local surface plasmon resonance [23–24]. More recently, TMPs have been applied for cancer photothermal therapy and CDT [25–27]. Currently, for TMPs, it is urgent to improve their reactive activity in the TME to improve cancer therapy.

On the other hand, Ca^{2+}, as an intracellular second messenger, can modulate a series of cell physiological processes. Because transmembrane Ca^{2+} channels are often overexpressed in many kinds of cancer cells, the cytosolic calcium concentration ($[Ca^{2+}]_i$) is increased to promote the Ca^{2+}-involved proliferative pathway. As a result, cancer cells are sensitive to changes in the $[Ca^{2+}]_i$ concentration, which can be considered an effective cancer therapeutic target [28]. Elevated $[Ca^{2+}]_i$ concentrations directly act on the mitochondrial membrane, causing functional changes and triggering the production of more ROS. In turn, mitochondrial damage and ROS elevation can modulate Ca^{2+} dynamics and augment the Ca^{2+} surge. This reciprocal interaction and feedback loop between the $[Ca^{2+}]_i$ concentration and mitochondrial ROS can trigger a butterfly effect to induce fatal cellular oxidative damage. We envision that the design of a nanoagent with the ability to trigger initial intracellular calcium elevation and ROS generation can provoke the butterfly effect.

In this study, we fabricated a $CaCO_3$ nanoshell mineralized cobalt phosphide nanocage (CoP@$CaCO_3$, CCP) with a hollow cube structure. $CaCO_3$, as a kind of natural biological mineral, has good biocompatibility [29–30]. Once endocytosed into tumor cells, the $CaCO_3$ nanoshell can be degraded under lysosome acidic conditions and release Ca^{2+} into the cells to elevate the intracellular Ca^{2+} concentration, which further switches on intracellular mitochondrial damage and ROS generation. Meanwhile, the exposed CoP nanocore with a porous hollow structure can fully expose cobalt (Co^{2+} and Co^{3+}) as Fenton-like reaction active sites to augment ·OH production. In the core, the heterogeneous *N*-doped carbon skeleton and multi-interfacial heterojunction can facilitate interfacial electron transfer to boost Fenton-like catalytic activity [31–35]. Moreover, the inherent properties of cobalt phosphide allow it to realize high Fenton-like reactive activity in a weakly acidic TME. The ·OH elevation in cells in turn promotes intracellular calcium overload. The propagation of calcium/ROS elevation can continuously proceed in cancer cells. Finally, the cascade synergism between intracellular calcium overload and ROS generation exponentially promotes cascade amplification of ROS production to lead to cell death. Meanwhile, it effectively triggers the ICD process to augment the antitumor immunological effect to further improve the therapeutic outcome (Scheme 1).

2. Materials and methods

2.1. Chemicals and reagents

All chemicals and solvents were analytically pure without any further purification. Co $(CH_3COO)_2$■$4H_2O$ (98%), K3[Co (CN)6] (99.95 %), polypyrrolidone (PVP) (Wt = 58 K_D), $CaCl_2$, NH_4HCO_3 and 3,3′,5,5′-tetramethylbenzidine (TMB) were purchased from Aladdin. Co., Ltd., and NaH_2PO_2 (AR) was purchased from Macklin, Co., Ltd. Cell Counting Kit-8 (CCK-8) was purchased from Dojindo Laboratories. Acetoxymethylester of calcein (Calcein-AM), propidium iodide (PI), 2,7-dichlorodihydrofluorescein diacetate (DCFH-DA), mitochondrial membrane potential assay kit with JC-1 were purchased from Beijing Solarbio Science & Technology Co., Ltd. Calreticulin rabbit monoclonal antibody and FITC labeled goat anti-rabbit IgG (H + L) were purchased from Beyotime Biotechnology Co. Mouse IL-6 Elisa kit, mouse TNF-α Elisa kit, TruStain fcX™ , APC anti-mouse CD4, PE anti-mouse CD80, APC anti-mouse CD86, FITC anti-mouse CD11c, FITC anti-mouse CD3, and PE anti-

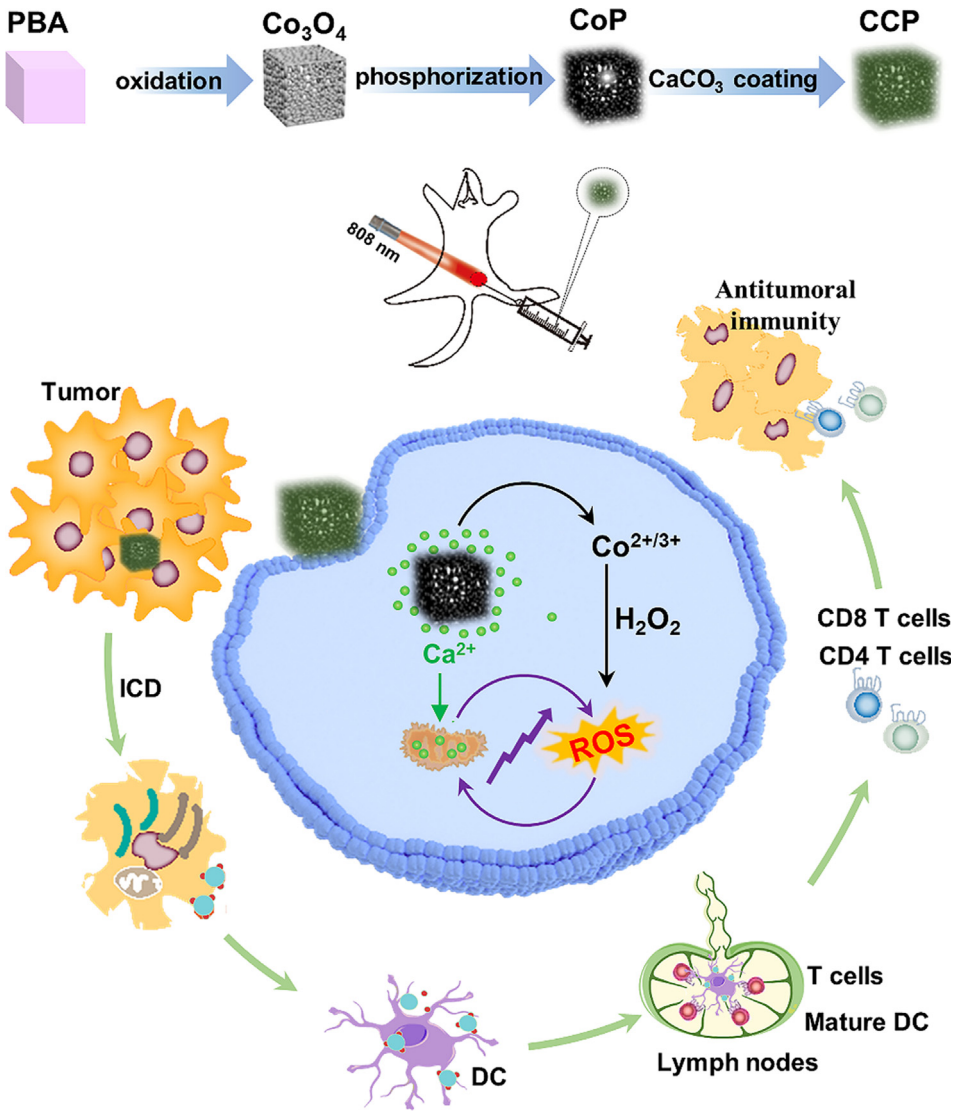

Scheme 1. Synthesis process of CCP and the schematic illustration of the calcium overload and photo-enhanced ROS generation for tumor therapy.

mouse CD8a were purchased from Shenzhen Dakowei Bioengineering Co., Ltd. Ammonium-chloride-potassium (ACK) lysing buffer was purchased from Invitrogen Co., Ltd.

2.2. Instruments

X-ray diffraction (XRD) data of the nanoparticles were detected by using Cu Kα (λ = 0.15406 nm) radiation on the D8 focusing diffractometer (Bruker D8 DISCOVER). The morphologies of the nanoparticles were acquired with a scanning electron microscope (SEM, Nova nanosem 450) and a transmission electron microscope (TEM, JEM-2100). UV–3600 (Shimadzu, Japan) was used to measure the UV–Vis absorption spectra. X-ray photoelectron spectroscopy (XPS, ESCALAB 250Xi) was used to measure the XPS spectra. Dynamic light scattering (DLS) size distribution and Zeta potential were obtained by using a Beckman coulter instrument (Delsamax Pro).

2.3. Synthesis of PBA

The Prussian blue derivative (PBA) was synthesized through the room-temperature reaction of $K_3[Co(CN)_6]$ with $Co(CH_3COO)_2{\cdot}4H_2O$. In detail, Co $(CH_3COO)_2{\cdot}4H_2O$ (0.0187 g) was completely dissolved in 10 mL deionized water to form homogenous solution A. Then, 0.0166 g $K_3[Co(CN)_6]$ and polypyrrolidone (0.3 g) were dissolved in 10 mL deionized water to form solution B. Solution A was added dropwise into solution B followed by stirring for 10 min and then aged at room temperature for 24 h. Then, the mixed solution was centrifuged to collect the sediment PBA and washed with ethanol and deionized water 6 times.

2.4. Synthesis of Co_3O_4 nanocage

The resultant PBA was calcined in air to obtain Co_3O_4 nanocubes. In detail, Co_3O_4 nanocages were synthesized by placing PBA in a tubular furnace, heated to 450 °C at a heating rate of 10 °C min^{-1}, and maintained for 1 h in air. The product was washed several times with deionized water.

2.5. Synthesis of CoP nanocage

NaH_2PO_2 (0.024 g) and Co_3O_4 nanocages (0.1584 g) were placed upstream and downstream of the porcelain vessel in a tubular furnace, respectively. Under a slow argon flow, the vessel was heated

to 320 °C at a heating rate of 1.5 °C min^{-1} and maintained at 320 °C for 60 min. After cooling to room temperature, the products were collected and washed several times with deionized water.

2.6. Synthesis of CCP

In a beaker, CoP nanocages (2 mg) were dispersed in 50 mL ethanol, and then $CaCl_2{\cdot}2H_2O$ (22 mg) was added. NH_4HCO_3 (5 g) was put into another beaker. The two beakers were placed close to each other in a vacuum drying oven at room temperature for 8 h to coat the $CaCO_3$ nanolayer on the CoP nanocage.

2.7. Photothermal conversion property

The photothermal conversion property was measured under an 808 nm laser irradiation. The temperature change was recorded by a HT9815 thermocouple. A total of 1 mL of CCP suspension in pH6.5 PBS with different concentrations was put in a quartz bottle and irradiated for 10 min, and the temperature change was recorded. The photothermal conversion efficiency (η) is calculated according to the following formula:

$$\eta = \frac{[hST_{\max} - T_{surr} - Q_{Dis}]}{[I1 - 10^{-A}]} \times 100\% \quad (1)$$

$$hS = (\sum m_i C_{pi})/\tau_s \quad (2)$$

$$t = \tau_s \times (-\ln\theta) \quad (3)$$

$$\theta = (T - T_{surr})/T_{\max} - T_{surr} \quad (4)$$

where h is the heat transfer coefficient, S is the irradiated area, T_{max} is the equilibrium temperature, T_{surr} is the ambient temperature, Q_{dis} was measured independently using a quartz bottle containing PBS (pH6.5), I is the laser power, C_p is 4.2 J• (g ° C)$^{-1}$, and τ_s is the sample system time constant.

2.8. •OH detection by electron spin resonance (ESR) spectroscopy

•OH was detected by spin detection using 5,5-dimethyl-1-pyrroline-*n*-oxide (DMPO) as the trapping agent. The groups that needing NIR were irradiated with 1 W cm^{-2} 808 nm laser.

2.9. The pH-responsive degradation of CCP

CCP (1 mg mL^{-1}) was suspended in 1 mL PBS at different pH values (7.4 and 6.5). After incubation for 4 h and 8 h, the morphology of CCP was observed using TEM, and the hydrodynamic diameter was determined by DLS.

2.10. Evaluation of Fenton-like reaction

The Fenton-like reaction to produce •OH was evaluated by a UV–vis spectrophotometer. Fifty milliliters of nanoparticles (1 mg mL^{-1}), 25 μL of TMB and 10 μL of H_2O_2 (30%) were added to 1 mL of pH buffer (pH = 4, 5, 6, 6.5, and 7). After reaction for 5 min, the mixture was centrifuged and the supernatant was measured on a UV–vis spectrophotometer.

2.11. Cell culture and cytotoxicity

Murine mammary carcinoma 4 T1 cells and murine fibroblast NIH-3 T3 cells (ATCC) were cultured in high-glucose Dulbecco's modified Eagle medium (DMEM) (Gibco), supplemented with 10% fetal bovine serum (FBS) and 1% penicillin/streptomycin. The cells were cultured at 37 °C in a humidified atmosphere of 5% CO_2. For detecting cytotoxicity, the cells were seeded on 96-well plates (8000 cells/well) and cultured for 12 h. The nanoparticles with different concentrations were added and cultured for additional 24 h. Then, the cytotoxicity was detected by CCK-8 assay kit. For the groups needing NIR, the cells were irradiated with an 808 nm laser (1 W cm^{-2}, 3 min) after the nanoparticles were added for 4 h.

2.12. In vivo systematic toxicity

The mice were randomly divided into four groups (n = 8). CCP dispersed in 100 μL PBS were intravenously injected into the mice with doses of 25, 50, and 100 mg kg^{-1}, respectively. The mice in the PBS group were injected with 100 μL PBS. Body weight was recorded every other day. After 14 days, blood was collected for routine blood test and blood biochemistry following standard procedures. The main organs including heart, liver, spleen, lung and kidney were collected and stained with hematoxylin and eosin (H&E) for histological examination.

2.13. Flow cytometry

4 T1 cells were cultured in Petri dishes. After different treatments, the cells were washed and stained with Hoechst 33,342 (5 μL) and PI (5 μL), and analyzed by flow cytometry (BD LSRFortessa). The data were analyzed by FlowJo-V10.

2.14. Live/dead staining

4 T1 cells in confocal dishes were incubated with CCP (100 μg mL^{-1}) for 24 h. After different treatments, Calcein-AM (2 mM) and PI (1.5 mM) were added and incubated with the cells for 25 min. After the cells were washed with PBS 3 times, the green (live cells) and red (dead cells) fluorescence were observed by CLSM (Leica SP8, Germany).

2.15. Intracellular ROS detection

4 T1 cells in confocal dishes were incubated with CCP (100 μg mL^{-1}) for 4 h. After different treatments, the cells were incubated with DCFH-DA at 37 °C for 15 min. After that, the cells were washed twice with PBS and imaged by CLSM.

2.16. Measurement of mitochondrial membrane potential (MMP, $\Delta\psi m$)

4 T1 cells in confocal dishes were incubated with CCP (100 μg mL^{-1}) for 4 h. After different treatments, the cells were incubated with JC-1 (10 μg mL^{-1}) at 37 °C for 15 min. Then, the cells were washed with PBS 3 times, and observed by CLSM.

2.17. Calreticulin (CRT) staining

4 T1 cells in confocal dishes were incubated with CCP (100 μg mL^{-1}) for 4 h. After different treatments, the cells were stained with CRT rabbit monoclonal antibody (1 mL, 1:200 diluted with PBS) overnight and washed with PBS 3 times. Then, the cells were incubated with goat anti-rabbit IgG (H + L) (1 mL, 1:200 diluted with PBS) for 2 h and washed with PBS 3 times. DAPI (10 μg mL^{-1}) was added to stain the nuclei. The green (CRT) and blue (nuclei) fluorescence were observed by CLSM.

2.18. Intracellular calcium staining

4 T1 cells in confocal dishes were incubated with CCP (100 μg mL^{-1}) for 4 h. After different treatments, the cells were

incubated with Fluo-4 AM (1 mL, 2 μM) at 37 °C for 30 min. Then, the cells were washed with PBS 3 times and observed by CLSM.

2.19. ROS levels in tumor tissues

After different treatments, the tumor tissues were snap-frozen, and 10 μm cryosections were prepared. The slices were fixed with acetone for 10 min, stained with DAPI (10 μg mL^{-1}) and DCFH-DA (20 μmol L^{-1}), and observed with CLSM (Leica SP8, Germany).

2.20. In vivo cancer therapy

The animal experiment was approved by the biomedical ethics committee of Peking University with approval No. LA2019128. 4 T1 cancer cells (10^6 cells) were subcutaneously injected into the left abdomen of the mice. After the tumor volume reached ~ 100 mm^3, the mice were randomly divided into 4 groups (n = 8): 1) PBS, 2) PBS + NIR, 3) CCP, and 4) CCP + NIR. CCP suspended in PBS at a dosage of 4 mg kg^{-1} was injected into tumors via local injection in the 3rd and 4th groups. Then, the mice in the 2nd and 4th groups were irradiated by an 808 nm laser (1 W cm^{-2}, 3 min) at the site of local tumor tissues. The weight and tumor size of the mice were recorded every two days. After 14 days, the mice were euthanized, and the tumors and important organs were removed for H&E staining. Tumor tissues were also stained with ki-67 via standard immunohistochemistry.

2.21. In vivo antitumor immunity

2.21.1. Cytokine

After 7 days of treatment, the whole blood of the mice was collected, and the serum was obtained by centrifugation. The concentrations of IL-6 and TNF-α in serum were analyzed via mouse IL-6 and TNF-α ELISA kits (n = 4), respectively.

2.21.2. Dendritic cell maturation and T-cell activation

After 7 days of treatment, in addition to collecting the whole blood of the mice, the tumor tissues of the mice were peeled, digested with collagenase and ground to obtain a single-cell suspension. To detect dendritic cell maturation, PE anti-mouse CD80 Ab, APC anti-mouse CD86 Ab, and FITC anti-mouse CD11c Ab were used to stain the cells, simultaneously. To detect *T*-cell activation, APC anti-mouse CD4 Ab, FITC anti-mouse CD3 Ab, and PE anti-mouse CD8a Ab were used to stain the cells, simultaneously. The stained cells were analyzed by flow cytometry. The data were analyzed by FlowJo-V10.

3. Results and discussion

3.1. Characterization

PBA nanoparticles have the advantages of adjustable structure, simple preparation, and good biocompatibility, and have been approved by the U.S. Food and Drug Administration as a kind of antidote. PBA was utilized as the precursor to synthesize CoP (Fig. 1a). From the TEM and SEM images, PBA had a uniform cubic morphology with a side length of 98.5 ± 5.5 nm (Fig. 1b and Figure S1a). The oxidized Co_3O_4 was a hollow nanocage with a reduced side length of 55.5 ± 4.5 nm (Fig. 1c and Figure S1b). Further phosphorization of the Co_3O_4 nanocage produced CoP nanocages with a slightly shrunken side length of 53.5 ± 2.5 nm (Fig. 1d and Figure S1c). The HRTEM image of the CoP nanocage showed well-resolved lattice fringes with distances of 1.74 Å, 3.64 Å, 2.52 Å, 2.72 Å and 2.43 Å, corresponding to the CoP (103), CoP_2 (111) (002), CoP_3 (220) and CoP_4 (310) crystal planes, respectively (Fig. 1e). Fig. 1f, Figure S1d and Figure S2 confirmed that an ultrathin $CaCO_3$ mineralized nanolayer (~5 nm) was successfully coated on the CoP nanocage to form $CaCO_3$@CoP. From the energy dispersive spectroscopy (EDS) element mapping of the CCP nanocage (Fig. 1g and 1 h), Co and P were mainly distributed in the core area, while Ca appeared in the outer nanoshell, further indicating the successful coating of the $CaCO_3$ nanolayer. According to the inductively coupled plasma mass spectrometer (ICP–MS), the atomic ratio of P, Ca, and Co was approximately 1:1.6:2.1.

The XRD patterns of the PBA and Co_3O_4 nanocages were consistent with previous reports (JCPDS No. 77–1161 and No. 42–1467, respectively) (Fig. 1i) [36]. After phosphorization, the CoP nanocage was composed of CoP_3 (cubic phase), CoP_4 (cubic phase), CoP (orthorhombic phase) and CoP_2 (monoclinic phase) (Fig. 1i). The surface electronic state of CoP was determined by XPS. The characteristic peaks of Co $2p_{1/2}$ (795.9 eV, 794.2 eV and 784.9 eV) and Co $2p_{3/2}$ (780.4 eV, 779 eV) illustrated that Co^{3+} and Co^{2+} coexisted (Fig. 1j) [38]. The binding energy of P $2p_{3/2}$ (129.1 eV) was lower than that of element P^0 (129.7 eV), indicating that P had a negative charge (Fig. 1k). The C 1 s spectrum deconvoluted at 283.6 eV, 284.3 eV, 285.5 eV and 287.4 eV corresponded to sp^2 hybrid C, sp^3 hybrid C—N, sp^3 hybrid C, and sp^2 hybrid C, respectively (Fig. 1l). The N 1 s peaks were well fitted with pyridine N (397.7 eV), pyrrole N (399 eV) and quaternary N (400 eV) (Fig. 1m). The presence of *N*-doped C provided more active sites for the redox reaction and was more conducive to charge transfer to facilitate CDT [39].

From the N_2 adsorption-desorption isotherm and pore size distribution, the CoP nanocage had a specific surface area of 65.2 m^2 g^{-1} and mesopores with sizes ranging from 2.2 nm to 9.2 nm (average size ~ 5.1 nm) (Fig. 1n and 1o). After $CaCO_3$ coating, the hydrodynamic diameter of CCP via DLS was slightly increased from 56.3 nm to 66.4 nm, and the zeta potential was changed from −58.2 mV to −35.7 mV, confirming the successful $CaCO_3$ coating (Fig. 1p and 1q).

From the Raman spectrum of the CoP nanocage (Figure S3), there were two C peaks at 1357 cm^{-1} and 1598 cm^{-1} corresponding to the D and G peaks, respectively. The I_D/I_G was calculated to be 1.15, indicating that a large number of atom defects were formed in CoP. Generally, the active catalytic atoms surrounding these defect sites have unsaturated chemical bonds, which change the surface electronic structure and available energy to enhance the chemical reactivity [37].

3.2. In vitro photoactivated cascade catalysis

The CCP nanocage showed improved light absorption, especially in the NIR light window (Fig. 2a). Under 808 nm laser irradiation, the CCP nanocage suspended in PBS showed a laser power density- and concentration- dependent photothermal conversion property (Fig. 2b and 2c). Under irradiation with an 808 nm laser (1 W cm^{-2}) for 10 min, the temperature for 50, 100 and 200 μg mL^{-1} CoP increased by 20.5 °C, 37.1 °C and 42.2 °C, respectively. The heating and cooling cycle experiments confirmed the stable photothermal conversion performance (Fig. 2d). The photothermal conversion efficiency (η) was calculated to be as high as 58.5%, which was obviously higher than that of the nonphosphatized Co_3O_4 nanocage (η = 25.12%) (Figure S5) and those previously reported metal phosphide nanoparticles (Table S1). Infrared thermal images also proved that CCP had a fast temperature increase during laser irradiation (Figure S6). The excellent photothermal conversion property was mainly due to the metal-like property and electron delocalization of metal phosphides [24].

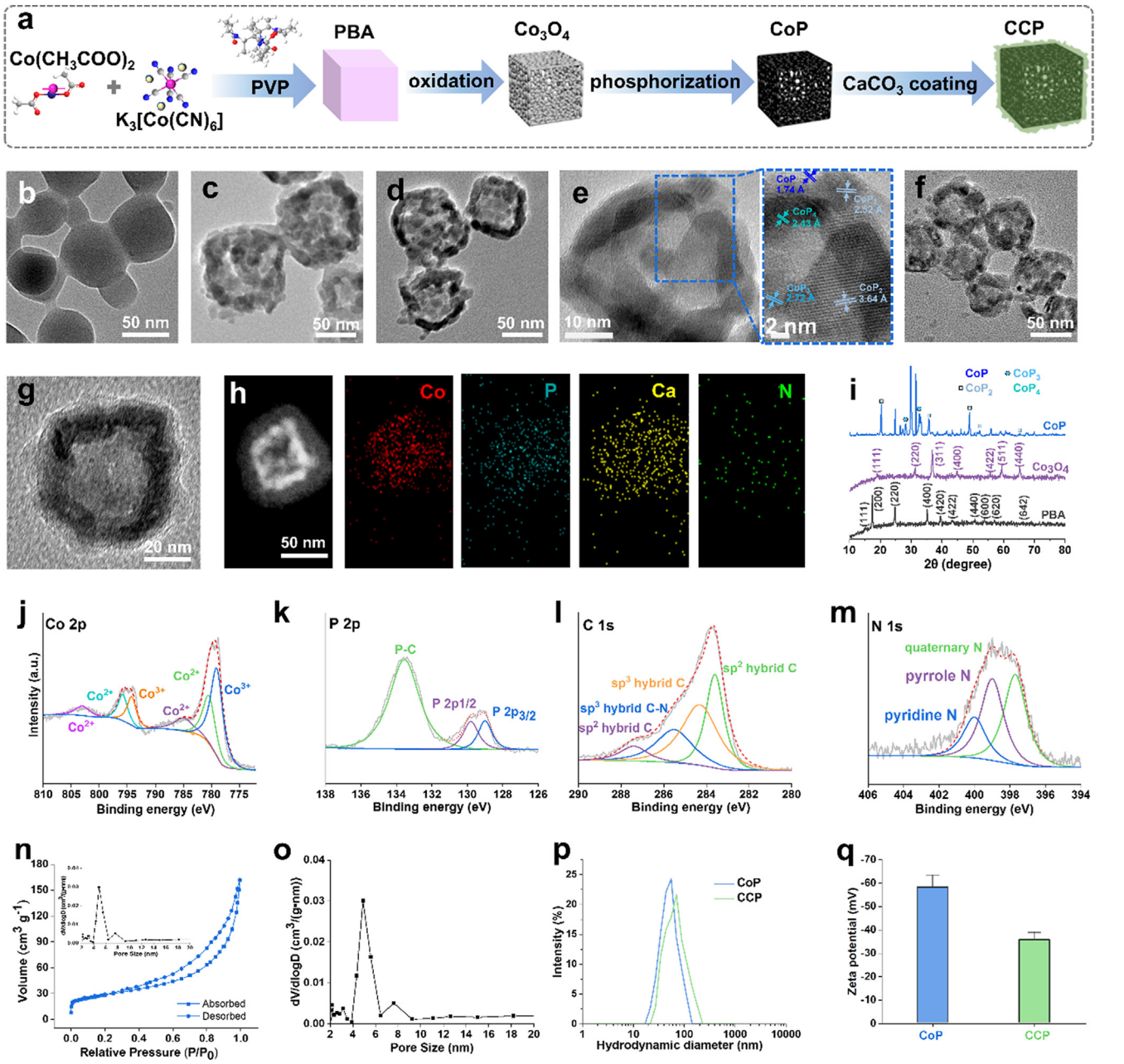

Fig. 1. The morphological and structural characterization. a) Schematic illustration of the synthetic procedure of CCP. TEM images of b) PBA, c) Co_3O_4, d) CoP, and e) CCP. f-g) STEM images of CCP and h) the EDS mapping for elements of Co, P, Ca, C and N. i) XRD patterns of the PBA, Co_3O_4 and CoP. XPS high-resolution scans of j) Co 2p, k) P 2p, l) C 1 s and m) N 1 s obtained from CoP. n) N_2 absorption-desorption isotherms and o) the corresponding pore size distribution of CoP. p) Hydrodynamic diameter distribution and q) zeta potential of CoP and CCP.

3.3. In vitro photoenhanced Fenton-like activity

The generation of OH is the key for the cell-killing effect of CDT. The CDT activity of CCP was detected through the oxidation of 3,3′,5,5′-tetramethylbenzidine (TMB) to blue-ox-TMB by the generated OH. With the addition of H_2O_2, CoP had a high Fenton-like reaction activity within a wide acidic pH range of 4 ∼ 6.5 (Fig. 2e). The highest reaction activity appeared at pH 4 for all the kinds of nanomaterials, under which pH the CCP's activity was higher than that of PBA and Co_3O_4 nanocages. More meaningfully, at a pH of 6.5, similar to that in the TME, the activity of CoP reached 66.26% of its highest activity at pH = 4. Instead, the activities of Co_3O_4 and PBA at pH 6.5 were only 16.45% and 24.58% of their highest activities at pH 4, respectively. Moreover, at neutral physiological pH 7.4, CoP had a relatively low reactive activity, ensuring its low toxicity in systematic circulation. Moreover, CoP had high catalytic activities over a broad range of temperatures from 25 to 50 °C (Fig. 2f). Therefore, under NIR light irradiation for photothermal conversion, the CDT efficiency can also be improved (Fig. 2g). Currently, one of the main obstacles for the application of CDT is that the designed nanoagents often have low activity at the mildly acidic pH of the TME and high toxicity under physiological conditions. The obvious difference in catalytic activity of CCP under TME and physiological conditions ensures its highly specific cancer therapy with low systematic toxicity.

Electron spin resonance (ESR) spectroscopy was also applied to detect OH using 5,5-dimethyl-1-pyrroline *N*-oxide (DMPO) as a capture probe. With the addition of H_2O_2 to the CCP suspension,

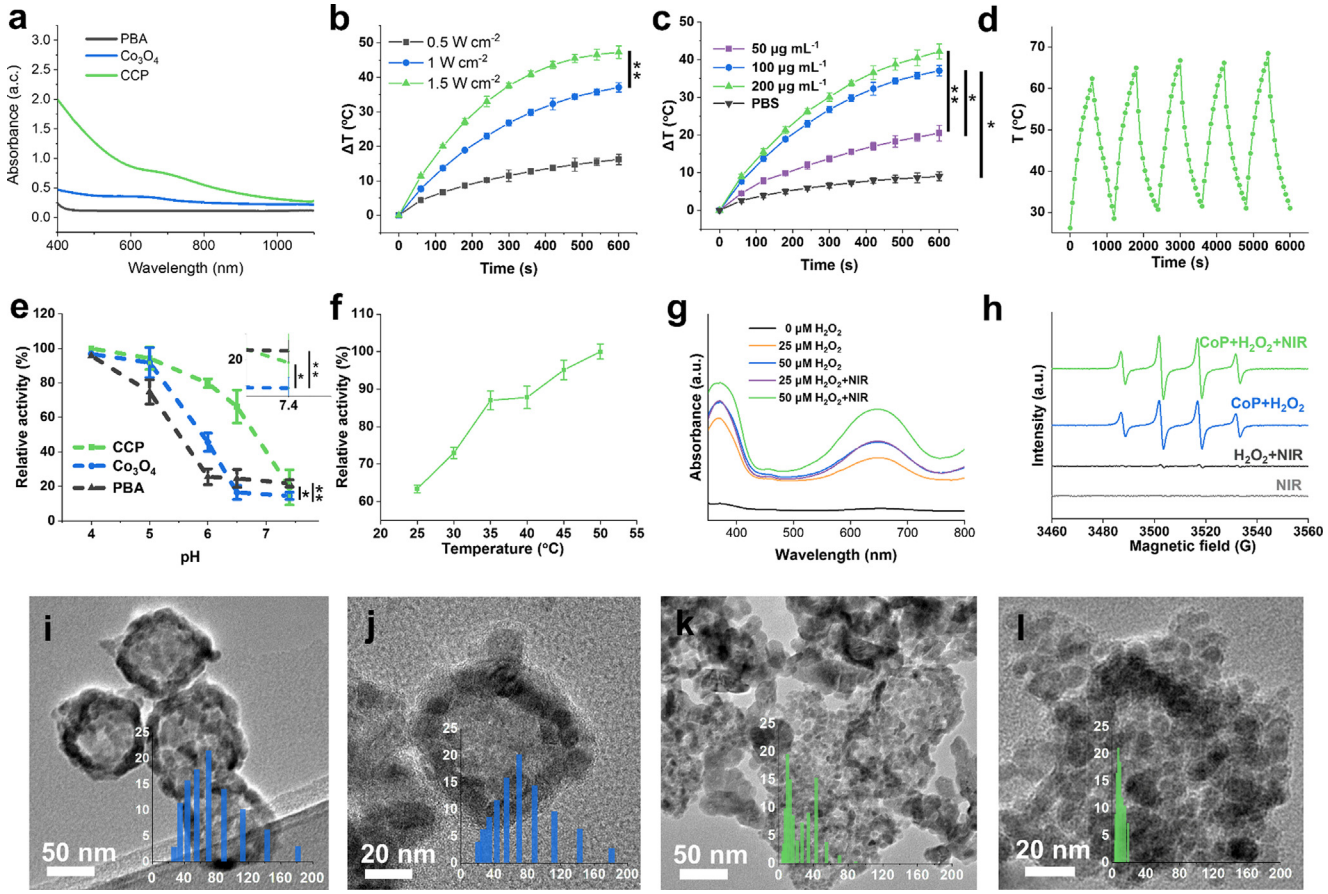

Fig. 2. Photothermal conversion, catalytic performance, and pH-responsive degradation of the CCP. a) UV–Vis absorption spectra of the PBA, Co_3O_4 and CCP. b) Photothermal conversion of CCP (100 μg mL^{-1}) irradiated by 808 nm laser (0.5, 1 and 1.5 W cm^{-2}) for 10 min, respectively. Test results derived from three independent measurements. c) Photothermal conversion of CCP with different concentrations (0, 50, 100 and 200 μg mL^{-1}) under 808 nm laser irradiation (1 W cm^{-2}, 10 min). Test results derived from three independent measurements. d) Cyclic heating and cooling curves of CCP. e) Comparison of POD-like activity of PBA, Co_3O_4 and CCP under different pH values. The catalytic activity of CCP at pH 4 was defined as 100%, and the activity of PBA and Co_3O_4 at other conditions was compared with it. The inset is a partial enlarged view of Fig. 2e. Test results derived from three independent measurements. f) Temperature-dependent POD-like activity of CCP. g) POD-like activity of CCP with different concentrations of H_2O_2 with or without 808 nm laser (1 W cm^{-2}, 3 min). h) The ESR spectra of DMPO/·OH generated by CCP. i to j) TEM images of CCP after incubation in PBS buffer of pH7.4 for i) 4 h and j) 8 h. k to l) TEM images of CCP after incubation in PBS buffer of pH6.5 for k) 4 h and l) 8 h. The insets in i-k show corresponding hydrodynamic diameter distribution.

characteristic peaks of ·OH with a peak intensity ratio of 1:2:2:1 can be observed (Fig. 2h). Moreover, under NIR light irradiation, the generation of ·OH was further improved.

We also detected morphological changes in CCP in media with different pH values. After 4 h and 8 h in physiological medium of pH 7.4, the CCP had no obvious change in morphology from the TEM observation. The hydrodynamic diameter was kept at 65.5 ± 1.5 nm at 8 h (Fig. 2i to 2j). In pH 6.5 medium, however, the structure of CCP collapsed after 4 h of incubation, and reassembled into large nano- to microsized agglomerates after 8 h. From the DLS result, the hydrodynamic diameter was 22.78 ± 17.62 nm at 4 h and changed to 9.63 ± 5.97 nm at 8 h (Fig. 2k to 2 l). This result demonstrated that CCP had good stability in a physiological environment and could be biodegraded in the TME to release Ca^{2+} and promote the Fenton-like reaction.

3.4. In vitro Fenton-like activity and cancer therapy

With these properties, we evaluated its cancer cell killing effect. The highly tumorigenic and invasive murine cell line 4 T1, a triple-negative breast cancer cell line and the human breast cancer cell line MCF-7 were used to evaluate the cell-killing effect, and human renal epithelial cells (293 T) were used as a representative normal cell line to evaluate biocompatibility via the cell counting kit 8 (CCK-8) assay. After treatment with uncoated CoP nanocages at a concentration of 200 μg mL^{-1} for 24 h, the survival rate of 293 T cells was only 11.2%. In comparison, the cells treated with CCP at the same concentration maintained a survival rate of 76.6% (Fig. 3a). This confirmed that the $CaCO_3$ nanolayer can improve the biocompatibility of the nanocages. For 4 T1 cells, the cell viability was 78.1% with 200 μg mL^{-1} CCP treatment (Fig. 3b). Without CCP, different treatments, including as high as 200 μM H_2O_2, pH 6.5 medium, and 808 nm laser irradiation (1 W cm^{-2}, 3 min) had no adverse influence on cell viability (Figure S7). Under this premise, the 4 T1 cells treated with 808 nm laser irradiation (1 W cm^{-2}, 3 min) after endocytosis of 200 μg mL^{-1} CCP (CCP + NIR group) had a survival rate of 48.2%. Moreover, the cells treated with 200 μg mL^{-1} CCP plus 100 μM H_2O_2 to simulate the overproduction of H_2O_2 in the TME (CCP + H_2O_2 group) had a survival rate of 81.7%. The simultaneous treatment of H_2O_2 and NIR light irradiation with 200 μg mL^{-1} CCP (CCP + H_2O_2 + NIR, pH 7.4) caused a further decrease in cell viability to 37.6%. To further simulate the mildly acidic TME, the cell activity at pH 6.5 was evaluated. At pH 6.5, the lowest cell survival rate of 7.8% was reached with 200 μg mL^{-1} CCP plus 100 μM H_2O_2 and laser irradiation (CCP + H_2O_2 + NIR, pH 6.5) (Fig. 3c). The cell-killing effect on MCF-7 was even higher than that on 4 T1 cells due to the higher malignance of 4 T1 as a kind of highly invasive and triple-

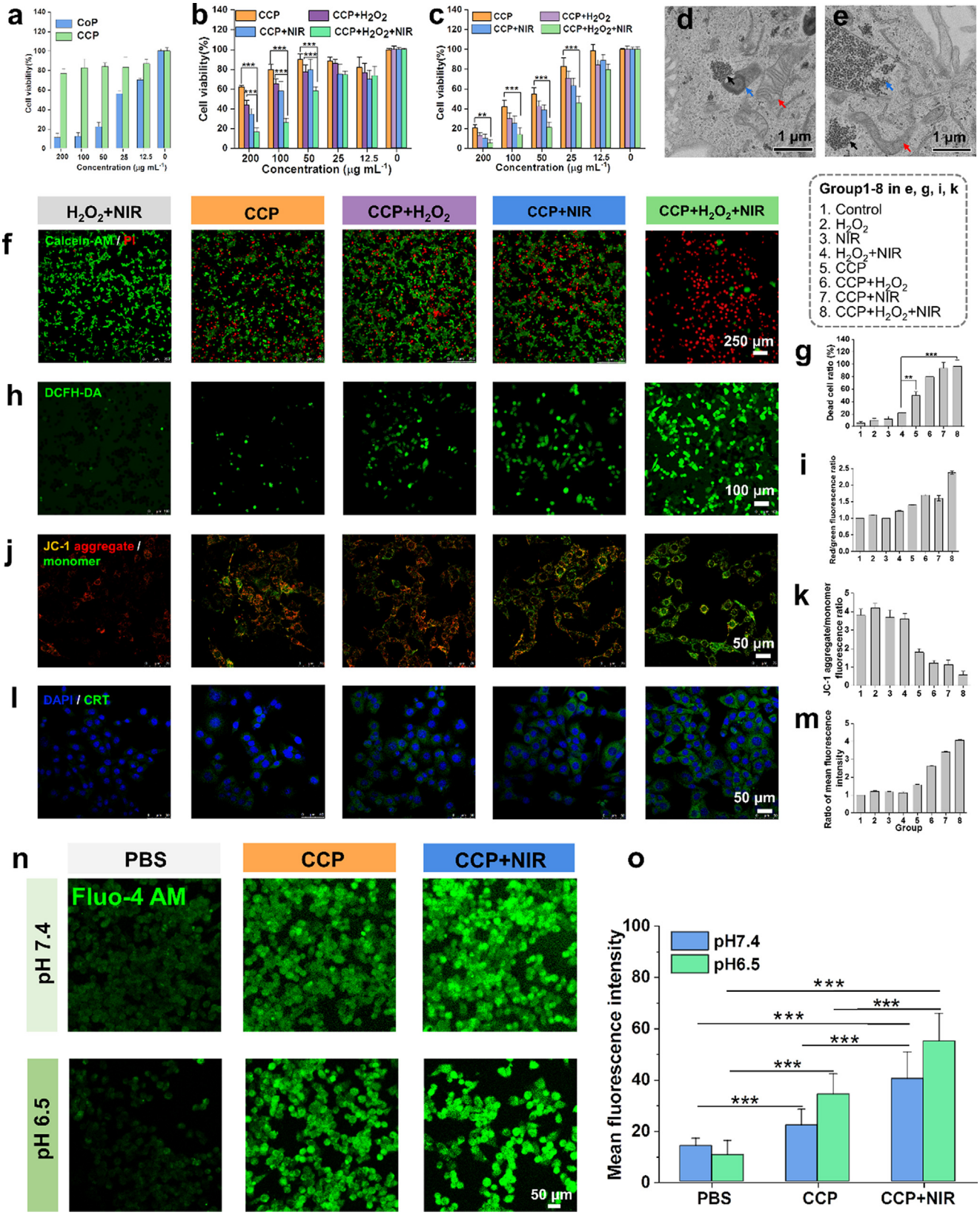

Fig. 3. Evaluation of the biocompatibility and therapeutic effect of CCP at cellular level. a) Viability of 293 T cells incubated with different concentrations of CCP for 24 h. b) Viability of 4 T1 cells incubated with different concentrations of CCP at pH 7.4 with or without H_2O_2 and NIR. c) Viability of 4 T1 cells incubated with different concentrations of CCP at pH 6.5 with or without H_2O_2 and NIR. d to e) TEM images of the cellular uptake of 4 T1 cells after co-incubation with CCP for d) 4 h and e) 12 h. f) Calcein-AM/PI staining after different treatments and g) the corresponding proportion of dead cells. h) Fluorescence images of intracellular ROS in 4 T1 cells detected by DCFH-DA and i) the radio of mean fluorescence intensity. Fluorescence in the untreated control group is set as 1. j) Fluorescence images of 4 T1 cells stained with JC-1 probe after different treatments and k) the corresponding JC-1 aggregate/monomer fluorescence ratio. l) CRT and nuclear staining after different treatments and m) the corresponding mean fluorescence intensity. n) Fluorescence images of 4 T1 cells stained with Fluo-4 AM as Ca^{2+} indicator after different treatments and o) the corresponding mean fluorescence intensity. Asterisks indicate significant differences (*p < 0.05, **p < 0.01, ***p < 0.001). Test results derived from three independent measurements.

negative breast cancer (Figure S8). We directly observed the endocytosis of CCP by 4 T1 cells via bio-TEM imaging. From the TEM images, after incubation of CCP for 4 h with the cells, many aggregated small nanoparticles with sizes of ~ 10 nm can be observed in bilayer membrane vesicles and cytoplasm (Fig. 3d). Importantly, after 12 h of endocytosis, the mitochondria of the cells had damaged structures, in which the inner mitochondrial membrane had been destroyed (Fig. 3e). The pathway of cell death was further studied by flow-cytometry apoptosis assays. After different treatments, 4 T1 cells were stained with Hoechst 33,342 and propidium iodide (PI). The cells in the PBS and PBS + NIR groups had low apoptosis and cell death. In contrast, the percent of cell apoptosis in the CCP and CCP + NIR groups was 6.9- and 25.29-fold higher than that in the PBS group, respectively (Figure S9), proving that the synergy of ROS production and PTT had the highest anticancer effect through cell apoptosis.

Calcein-AM/propidium iodide (PI) staining was employed tintuitively distinguish between living and dead cells. Dead cells in the H_2O_2 + NIR, CCP, CCP + H_2O_2, CCP + NIR, and CCP + H_2O_2 + NIR groups comprised 22.1%, 50.1%, 80.3%, 93.5% and 96.5% of the total cells, respectively (Fig. 3f-g). For the intracellular ROS level stained with 2,7-dichlorofluorescin diacetate (DCFH-DA), the cells in the H_2O_2 + NIR, CCP, CCP + H_2O_2, CCP + NIR, and CCP + H_2O_2 + NIR groups showed 1.2-, 1.4-, 1.7-, 1.6-, and 2.38-fold fluorescence increases compared to the untreated control cells, respectively (Fig. 3h and 3i). Moreover, cell mitochondrial membrane potential (MMP) was detected with 5,5′,6,6′-tetrachloro-1,1′,3,3′-tetraethyl benzimidazolyl carbocyanine-iodide (JC-1) to predict cellular oxidative damage [33], in which the ratio of red fluorescence (J-aggregates represent high MMP) to green fluorescence (monomeric form represents low MMP) reflects the value of MMP. Cells in the high-viability control groups (control, H_2O_2, NIR and H_2O_2 + NIR groups) mainly showed red fluorescence, whose green fluorescence signals could be nearly ignored (Figure S10). In the CCP, CCP + H_2O_2, CCP + NIR, and CCP + H_2O_2 + NIR groups, the red:green fluorescence ratio decreased by 0.47-, 0.31-, 0.29- and 0.15- fold, respectively, relative to the PBS group (Fig. 3j and 3 k). The decreased MMP indicated that the mitochondrial membrane was depolarized, which would finally result in mitochondrial dysfunction and cellular oxidative damage. All the results proved that under TME conditions, with the synergy of photothermal effects promoting Fenton-like activities, CCP can kill cancer cells by the production of ROS to induce and mitochondrial dysfunction and cellular oxidative damage.

Synergetic therapy can also trigger ICD. In the treatment process, killed cancer cells can release or expose antigens, such as calreticulin (CRT), as the "eat me" signal of phagocytosis, which can further activate the innate immune system, stimulate tumor specific T cells, and improve the therapeutic outcome [40–43]. From the immunofluorescent staining images, the exposed CRT in the CCP, CCP + H_2O_2, CCP + NIR, and CCP + H_2O_2 + NIR groups had 1.57-, 2.63-, 3.42- and 4.08-fold increases compared with the control group, respectively, suggesting that both photothermal effects and Fenton-like reactions can promote the exposure of CRT to stimulate further antitumor immunity (Fig. 3l and 3 m).

After confirming the acid-triggered biodegradation, the intracellular Ca^{2+} ($[Ca^{2+}]_i$) was assessed using Fluo-4 AM as the Ca^{2+} indicator (Fig. 3n). In pH 7.4 medium, the cells with coincubation of CCP for 4 h and those with CCP coincubation and additional NIR laser irradiation (CCP + NIR group) had increased $[Ca^{2+}]_i$ concentrations by 1.57- and 2.87-fold, respectively (Fig. 3o). When the cell culture media was changed to pH 6.5, the $[Ca^{2+}]_i$ concentration was further increased. These results suggested that CCP treatment, NIR laser irradiation, and pH decrease can all activate intracellular Ca^{2+} elevation, and lead to amplification of ROS generation and cellular oxidative damage.

3.5. In vivo cancer therapy

With the excellent therapeutic effect at the cellular level having been established, we further evaluated the in vivo cancer therapeutic effect. 4 T1 cells were used as the model of typical triple-negative breast cancer, which is a refractory breast cancer with high metastasis and mortality, low responsiveness to various clinical therapies, and poor prognosis.

First, intravenous administration of high-dose CCP up to 100 mg kg^{-1} into the mice did not induce any observable toxic response from the results of histopathological analysis of the main tissues, blood biochemical analysis, and routine blood tests (Figure S11-13). Furthermore, tumor slices were stained with DAPI and DCFH-DA to characterize the ROS level in cancer cells in vivo. In the CCP and CCP + NIR groups, ROS levels were significantly higher than those in the PBS and PBS + NIR groups (Figure S14). This result was consistent with that in the cell experiments, suggesting that CCP can result in high ROS production at tumor sites. For in vivo antitumor therapy, 4 T1 tumor-bearing BALB/c mice were used and treated through intratumoral administration of CCP with or without further NIR light irradiation. The experimental protocol and time schedule are shown in Fig. 4a. Briefly, when the tumor volume reached approximately 100 mm^3, 4 T1-tumor-bearing BALB/c female mice were randomly divided into 4 groups (n = 8): 1) PBS group: only PBS injection; 2) PBS + NIR group: NIR light irradiation after PBS injection; 3) CCP group: CCP injection; 4) CCP + NIR group: NIR light irradiation after CCP injection. On the 2nd and 4th, the local tumor tissues were irradiated with an 808 nm laser at 1 W cm^{-2} for 3 min. During laser irradiation in the CCP + NIR group, the temperature at the tumor site increased to 53.5 °C, as detected by an infrared thermal imager (Fig. 4b and 4c). During the 14-day treatment, none of the mice showed a change in body weight (Fig. 4d). At the end of the therapy, mouse tumors in the CCP group were remarkably inhibited, and those in the CCP + NIR group were almost cured (Fig. 4e and 4f). The tumor inhibition rates for the CCP and CCP + NIR groups were calculated to be 76.5% and 99.6%, respectively. In the CCP group, the tumors of two mice disappeared (25% of the mice), and the tumors of six mice in the CCP + NIR group disappeared completely (75% of the mice). Hematoxylin and eosin (H&E) staining showed that the main organs, including the heart, liver, spleen, lung and kidney, no abnormalities in any of the treated mice (Figure S14). In the CCP and CCP + NIR groups, the malignant cells in the stripped tissues were greatly reduced and completely disappeared, respectively, compared with the control group (Fig. 4g). Immunohistochemistry for ki-67, a cell cycle-associated protein and proliferation marker, showed similar results. It should be mentioned that because some tumor tissues in the CCP + NIR group were unfindable, the tissues peeled from the surroundings of the initial tumor location were examined instead.

3.6. Antitumor immunity

ICD was also examined in the in vivo cancer therapy. With the exposed cellular antigen being presented to DC cells, the mature DC cells can further activate T cells into cytotoxic T cells or helper T cells that can be recruited to kill the cancer cells [44–47]. Meanwhile, some proinflammatory cytokines might be secreted, such as interleukin-6 (IL-6) and tumor necrosis factor-α (TNF-α). IL-6 plays an important role in the anti-infection immune response, and TNF-α, as a kind of tumor necrosis factor, can kill tumor cells directly. The levels of intratumoral immune cells and IL-6 and TNF-α in serum were detected to evaluate the antitumor immunological effect after 7 days of different treatments. The maturation of DCs was examined by staining the cell surface markers CD11c, CD80 and CD86 using flow cytometry. The $CD11c^+CD86^+CD80^+$ cells rep-

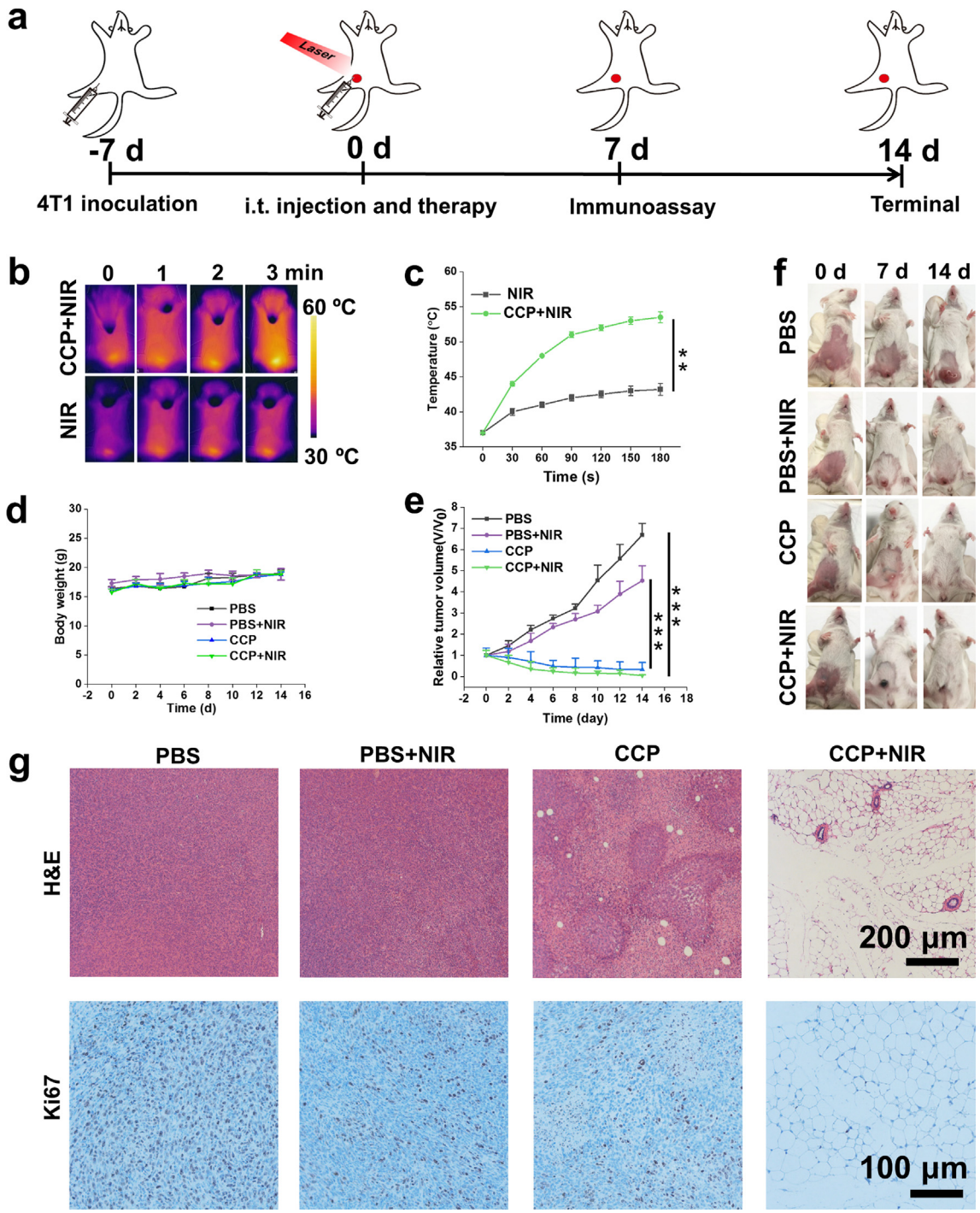

Fig. 4. In vivo therapeutic evaluation of CCP. a) Experimental timetable for the therapy process. b) Near infrared photothermal imaging of 4 T1-bearing mice injected with CCP (5 mg kg^{-1}, 70 μL) and c) corresponding temperature curve. The tumor site is exposed to an 808 nm NIR laser at 1 W cm^{-2} for 3 min. Test results derived from three independent measurements. d) Changes of body weight and e) tumor volume growth curve of 4 T1-bearing mice in different groups during therapeutic period. Test results derived from three independent measurements. f) Representative photographs of the mice after different treatments. Asterisks indicate significant differences (*p < 0.05, **p < 0.01, ***p < 0.001). g) H&E staining and ki-67 immunohistochemistry of tumor tissues in different groups at the terminal of the therapy.

resenting mature DCs in the CCP + NIR group were 10.7% of the total $CD11c^+$ DCs, which was 1.71-, 1.45-, and 1.22– fold the levels found in the control (6.24%), NIR (7.36%), and CuFeP groups (8.72%), respectively (Fig. 5a). The cytotoxic T cells ($CD3^+CD8a^+$) and helper T cells ($CD3^+CD4^+$) in the CCP + NIR group were 16.6% and 32.8% of the total $CD3^+$ T cells, which were 1.47- and 1.51- fold of those in the PBS group, respectively (Fig. 5b and 5c).

For cytokines in the mouse serum, the IL-6 concentrations in the CCP (188.6 pg mL^{-1}) and CCP + NIR groups (287.5 pg mL^{-1}) increased by 1.20- and 1.83- fold , respectively, compared to those in the PBS group (157.7 pg mL^{-1}) (Fig. 5d). TNF-α secretions in the CCP group (16.55 pg mL^{-1}) and CCP + NIR group (28.62 pg mL^{-1}) were 1.56- and 2.69- fold those in the PBS group (10.62 pg mL^{-1}), respectively (Fig. 5e). Collectively, these results highlighted the great prospect of TME-responsive nanocages with the ability to trigger ROS generation and calcium overload to synergistically activate the ICD process to boost the therapeutic efficacy in murine models.

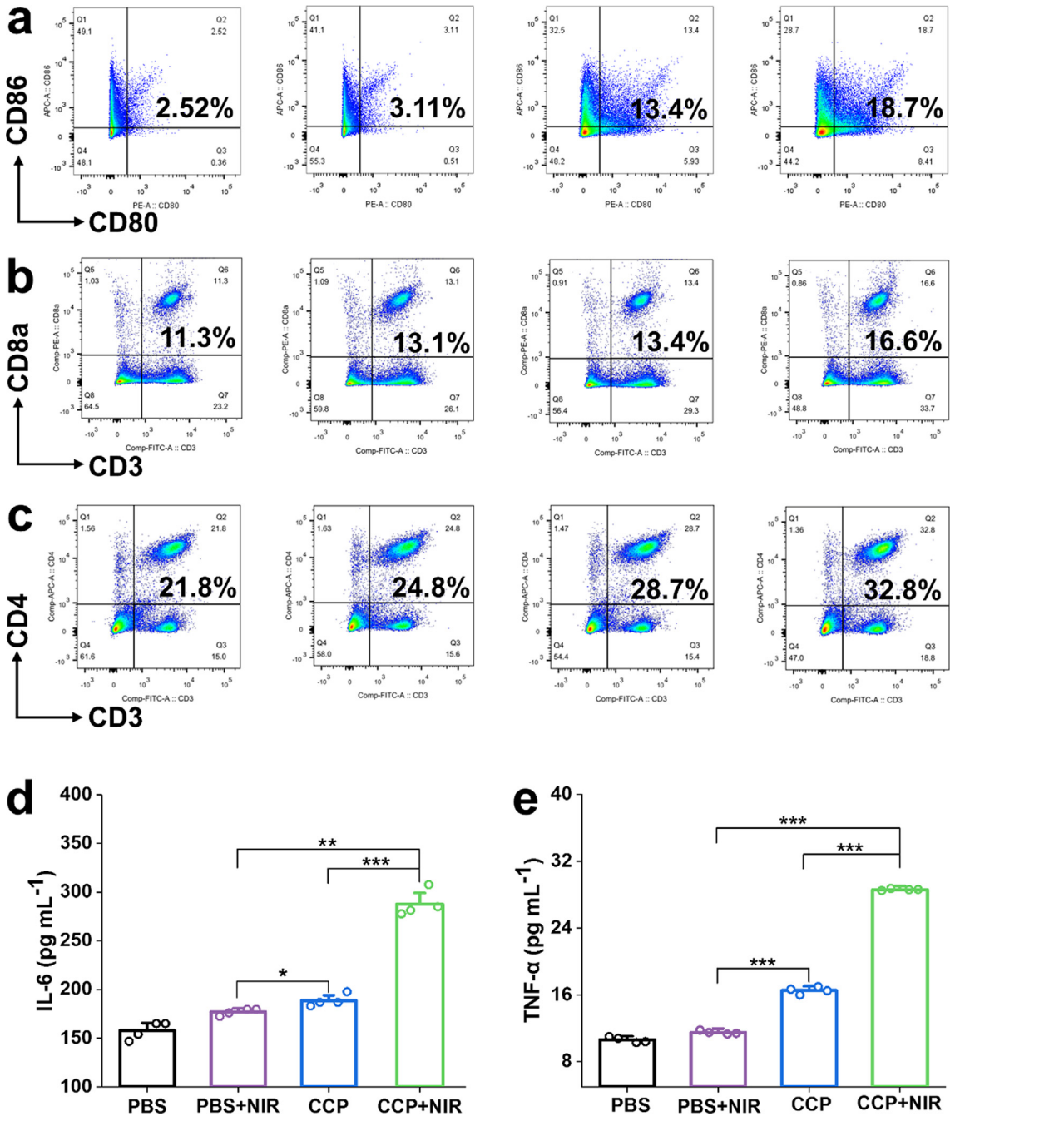

Fig. 5. In vivo ICD antitumor immunity. a) Flow cytometry data of the expression of CD80 and CD86 on the surface of dendritic cells after different treatments. b to c) Flow cytometry analysis of b) $CD4^+$ (marked by $CD3^+$ $CD4^+$) and c) $CD8^+$ (marked by $CD3^+$ $CD8^+$) T cell populations in the mice tumors after different treatments. d) Cytokine levels of IL-6 and e) TNF-α in the serum of the mice after different treatments. Test results derived from three independent measurements.

4. Conclusion

In summary, triggered by intracellular calcium signaling cascades, a core-shell CCP nanocage composed of mineralized $CaCO_3$ nanoshells and CoP nanocages as cores was fabricated. The $CaCO_3$@CoP nanocage can respond to weakly acidic pH and trigger reciprocal interactions and feedback loops between calcium overload and photoenhanced ROS generation [38–39]. All the experimental results indicated that in TME, compared with the previously reported CDT nanoagents, $CaCO_3$@CoP nanocage had higher Fenton-like reaction efficiency and better antitumor effect in synergy with calcium overload [29–30]. That is, the $CaCO_3$ nanoshell protects the core to improve biocompatibility under physiological conditions, and can be degraded once endocytosed into cancer cells to release Ca^{2+}, induce intracellular Ca^{2+} elevation, and trigger mitochondrial ROS generation. The synergetic propagation of calcium/ROS elevation, which also triggers the ICD process with antitumor immunity, can finally defeat the powerful and upregulated cellular antioxidant defensive system to defeat high-malignancy cancer. Overall, with rational design of the pH-responsive core-shell nanoagent, this work demonstrates an alternative strategy for enhancing CDT with remarkable synergistic performance to conquer cancer in murine models. This study paves a new pathway to augment ROS generation to improve cancer therapy.

CRediT authorship contribution statement

Xingru Zhao: Investigation, Methodology, Data curation, Writing – original draft. **Xingyi Wan:** Data curation. **Tian Huang:** Methodology. **Shuncheng Yao:** Software. **Shaobo Wang:** Investigation. **Yiming Ding:** Methodology. **Yunchao Zhao:** . **Zhou Li:** Investigation. **Linlin Li:** Resources, Conceptualization, Funding acquisition, Writing – review & editing.

Declaration of Competing Interest

The authors declare that they have no known competing financial interests or personal relationships that could have appeared to influence the work reported in this paper.

Acknowledgements

The work was supported by the National Nature Science Foundation (No. 82072065, 81471784), the National Key R&D project from Minister of Science and Technology, China (2016YFA0202703), and the National Youth Talent Support Program.

Appendix A. Supplementary material

Supplementary data to this article can be found online at https://doi.org/10.1016/j.jcis.2022.03.084.

References

[1] Y. Wang, R. Cai, C. Chen, The nano-bio interactions of nanomedicines: understanding the biochemical driving forces and redox reactions, Acc. Chem. Res. 52 (2019) 1507–1518.
[2] K. Fan, J. Xi, L. Fan, P. Wang, C. Zhu, Y. Tang, X. Xu, M. Liang, B. Jiang, X. Yan, L. Gao, In vivo guiding nitrogen-doped carbon nanozyme for tumor catalytic therapy, Nat. Commun. 9 (2018) 1440.
[3] B. Jiang, D. Duan, L. Gao, M. Zhou, K. Fan, Y. Tang, J. Xi, Y. Bi, Z. Tong, G.F. Gao, N. i. Xie, A. Tang, G. Nie, M. Liang, X. Yan, Standardized assays for determining the catalytic activity and kinetics of peroxidase-like nanozymes, Nat. Protoc. 13 (7) (2018) 1506–1520.
[4] K. Ai, J. Huang, Z. Xiao, Y. Yang, Y. Bai, J. Peng, Localized surface plasmon resonance properties and biomedical applications of copper selenide nanomaterials, Mater. Today Chem. 20 (2021) 100402.
[5] L. Feng, R. Xie, C. Wang, S. Gai, F. He, D. Yang, P. Yang, J. Lin, Magnetic targeting, tumor microenvironment-responsive intelligent nanocatalysts for enhanced tumor ablation, ACS Nano 12 (11) (2018) 11000–11012.
[6] B. Ma, S. Wang, F. Liu, S. Zhang, J. Duan, Z. Li, Y. Kong, Y. Sang, H. Liu, W. Bu, L. Li, Self-assembled copper-amino acid nanoparticles for in situ glutathione "AND" H_2O_2 sequentially triggered chemodynamic therapy, J. Am. Chem. Soc. 141 (2) (2019) 849–857.
[7] H. Zhang, J. Li, Y. Chen, J. Wu, K. Wang, L. Chen, Y.a. Wang, X. Jiang, Y. Liu, Y. Wu, D. Jin, W. Bu, Magneto-electrically enhanced intracellular catalysis of FePt-FeC heterostructures for chemodynamic therapy, Adv. Mater. 33 (17) (2021) e2100472.
[8] X. Zhao, S. Yao, X. Wan, T. Huang, Z. Zhang, X. Wang, S. Wang, Q. Liang, Z. Li, L. Li, Immunostimulatory multi-interfacial bimetallic phosphide nanoparticles as photo-enhanced cascade nanozyme for cancer therapy, Appl. Mater. Today 25 (2021) 101255.
[9] L.-S. Lin, J. Song, L. Song, K. Ke, Y. Liu, Z. Zhou, Z. Shen, J. Li, Z. Yang, W. Tang, G. Niu, H.-H. Yang, X. Chen, Simultaneous Fenton-like Ion delivery and glutathione depletion by MnO2 -based nanoagent to enhance chemodynamic therapy, Angew. Chem., Int. Ed. Engl. 57 (18) (2018) 4902–4906.
[10] M. Chang, M. Wang, M. Wang, M. Shu, B. Ding, C. Li, M. Pang, S. Cui, Z. Hou, J. Lin, A multifunctional cascade bioreactor based on hollow-structured Cu_2MoS_4 for synergetic cancer chemo-dynamic therapy/starvation therapy/phototherapy/immunotherapy with remarkably enhanced efficacy, Adv. Mater. 31 (51) (2019) e2100472.
[11] Y. Liu, J. Wu, Y. Jin, W. Zhen, Y. Wang, J. Liu, L. Jin, S. Zhang, Y. Zhao, S. Song, Y. Yang, H. Zhang, Copper(I) phosphide nanocrystals for in situ self-generation magnetic resonance imaging-guided photothermal-enhanced chemodynamic synergetic therapy resisting deep-seated tumor, Adv. Funct. Mater. 29 (2019) 1904678.
[12] S. Li, Y. Zhang, S.-H. Ho, B. Li, M. Wang, X. Deng, N.a. Yang, G. Liu, Z. Lu, J. Xu, Q. Shi, J.-Y. Han, L. Zhang, Y. Wu, Y. Zhao, G. Nie, Combination of tumour-infarction therapy and chemotherapy via the co-delivery of doxorubicin and thrombin encapsulated in tumour-targeted nanoparticles, Nat. Biomed. Eng. 4 (7) (2020) 732–742.
[13] M. Huo, L. Wang, Y. Chen, J. Shi, Tumor-selective catalytic nanomedicine by nanocatalyst delivery, Nat. Commun. 8 (2017) 357.
[14] K.F. Chu, D.E. Dupuy, Thermal ablation of tumours: biological mechanisms and advances in therapy, Nat. Rev. Cancer 14 (3) (2014) 199–208.
[15] M.Z. Dewan, A.E. Galloway, N. Kawashima, J.K. Dewyngaert, J.S. Babb, S.C. Formenti, S. Demaria, Fractionated but not single-dose radiotherapy induces an immune-mediated abscopal effect when combined with anti-CTLA-4 antibody, Clin. Cancer Res. 15 (17) (2009) 5379–5388.
[16] Z. Tang, P. Zhao, H. Wang, Y. Liu, W. Bu, Biomedicine meets Fenton chemistry, Chem. Rev. 121 (4) (2021) 1981–2019.
[17] X. Pan, W. Wang, Z. Huang, S. Liu, J. Guo, F. Zhang, H. Yuan, X. Li, F. Liu, H. Liu, MOF-derived double-layer hollow nanoparticles with oxygen generation ability for multimodal imaging-guided sonodynamic therapy, Angew. Chem., Int. Ed. Engl. 59 (32) (2020) 13557–13561.
[18] Y. Li, T. Gong, H. Gao, Y. Chen, H. Li, P. Zhao, Y. Jiang, K. Wang, Y. Wu, X. Zheng, W. Bu, ZIF-based nanoparticles combine X-ray-induced nitrosative stress with autophagy management for hypoxic prostate cancer therapy, Angew. Chem., Int. Ed. Engl. 60 (28) (2021) 15472–15481.
[19] C. Corbet, O. Feron, Tumour acidosis: from the passenger to the driver's seat, Nat. Rev. Cancer 17 (2017) 577–593.
[20] Z. Liu, S. Yang, B. Sun, P. Yang, J. Zheng, X. Li, Low-temperature synthesis of honeycomb CuP_2 @C in molten $ZnCl_2$ Salt for high-performance lithium ion batteries, Angew. Chem., Int. Ed. Engl. 59 (5) (2020) 1975–1979.
[21] S. Ji, B. Jiang, H. Hao, Y. Chen, J. Dong, Y.u. Mao, Z. Zhang, R. Gao, W. Chen, R. Zhang, Q. Liang, H. Li, S. Liu, Y.u. Wang, Q. Zhang, L. Gu, D. Duan, M. Liang, D. Wang, X. Yan, Y. Li, Matching the kinetics of natural enzymes with a single-atom iron nanozyme, Nat. Catal. 4 (5) (2021) 407–417.
[22] X.K. Wei, G. Bihlmayer, X. Zhou, W. Feng, Y.V. Kolen'ko, D. Xiong, L. Liu, S. Blügel, R.E. Dunin-Borkowski, Discovery of real-space topological ferroelectricity in metallic transition metal phosphides, Adv. Mater. 32 (2020) 2003479.
[23] X.F. Lu, L. Yu, X.W.D. Lou, Highly crystalline Ni-doped FeP/carbon hollow nanorods as all-pH efficient and durable hydrogen evolving electrocatalysts, Sci. Adv. 5 (2019) eaav6009.
[24] D. Chen, Z. Pu, R. Lu, P. Ji, P. Wang, J. Zhu, C. Lin, H.W. Li, X. Zhou, Z. Hu, F. Xia, J. Wu, S. Mu, Ultralow Ru loading transition metal phosphides as high-efficient bifunctional electrocatalyst for a solar-to-hydrogen generation system, Adv. Energy. Mater. 10 (2020) 2000814.
[25] X. Chu, X. Jiang, Y. Liu, S. Zhai, Y. Jiang, Y. Chen, J. Wu, Y. Wang, Y. Wu, X. Tao, X. He, W. Bu, Nitric oxide modulating calcium store for Ca^{2+}-initiated cancer therapy, Adv. Funct. Mater. 31 (2021) 2008507.
[26] Y. Liu, W. Zhen, Y. Wang, J. Liu, L. Jin, T. Zhang, S. Zhang, Y. Zhao, S. Song, C. Li, J. Zhu, Y. Yang, H. Zhang, One-dimensional Fe_2P acts as a Fenton agent in response to NIR II light and ultrasound for deep tumor synergetic theranostics, Angew. Chem., Int. Ed. Engl. 58 (2019) 2407–2412.
[27] Y. Liu, W. Zhen, Y. Wang, J. Liu, L. Jin, T. Zhang, S. Zhang, Y. Zhao, N.a. Yin, R. Niu, S. Song, L. Zhang, H. Zhang, Double switch biodegradable porous hollow trinickel monophosphide nanospheres for multimodal imaging guided photothermal therapy, Nano Lett. 19 (8) (2019) 5093–5101.
[28] S. Wang, X.i. Liu, S. Chen, Z. Liu, X. Zhang, X.-J. Liang, L. Li, Regulation of Ca(2+) signaling for drug-resistant breast cancer therapy with mesoporous silica nanocapsule encapsulated doxorubicin/siRNA cocktail, ACS Nano 13 (1) (2019) 274–283.
[29] Z. Yi, Z. Luo, N.D. Barth, X. Meng, H. Liu, W. Bu, A. All, M. Vendrell, X. Liu, In vivo tumor visualization through MRI off-on switching of $NaGdF_4$ -$CaCO_3$ nanoconjugates, Adv. Mater. 31 (37) (2019) 1901851.
[30] N. Hempel, M. Trebak, Crosstalk between calcium and reactive oxygen species signaling in cancer, Cell Calcium 63 (2017) 70–96.
[31] Z. Tang, Y. Liu, M. He, W. Bu, Chemodynamic therapy: tumour microenvironment-mediated Fenton and Fenton-like reactions, Angew. Chem., Int. Ed. Engl. 58 (2019) 946–956.
[32] Y.u. Chao, L. Xu, C. Liang, L. Feng, J. Xu, Z. Dong, L. Tian, X. Yi, K. Yang, Z. Liu, Combined local immunostimulatory radioisotope therapy and systemic immune checkpoint blockade imparts potent antitumour responses, Nat. Biomed. Eng. 2 (8) (2018) 611–621.
[33] L. Li, C. Chen, H. Liu, C. Fu, L. Tan, S. Wang, S. Fu, X.i. Liu, X. Meng, H. Liu, Multifunctional carbon-silica nanocapsules with gold core for synergistic photothermal and chemo-cancer therapy under the guidance of bimodal imaging, Adv. Funct. Mater. 26 (24) (2016) 4252–4261.
[34] L. Li, S. Fu, C. Chen, X. Wang, C. Fu, S. Wang, W. Guo, X. Yu, X. Zhang, Z. Liu, J. Qiu, H. Liu, Microenvironment-driven bioelimination of magnetoplasmonic nanoassemblies and their multimodal imaging-guided tumor photothermal therapy, ACS Nano 10 (7) (2016) 7094–7105.
[35] H. Dai, Q. Shen, J. Shao, W. Wang, F. Gao, X. Dong, Small molecular NIR-II fluorophores for cancer phototheranostics, The Innovation 2 (2021) 100082.
[36] J. Tian, H. Zhu, J. Chen, X. Zheng, H. Duan, K. Pu, P. Chen, Cobalt phosphide double-shelled nanocages: broadband light-harvesting nanostructures for efficient photothermal therapy and self-powered photoelectrochemical biosensing, Small 13 (2017) 1700798.
[37] L. Yan, F. Zhao, J. Wang, Y. Zu, Z. Gu, Y. Zhao, A safe-by-design strategy towards safer nanomaterials in nanomedicines, Adv. Mater. 31 (45) (2019) e1805391.
[38] J. Liu, L. Jin, Y. Wang, X. Ding, S. Zhang, S. Song, D. Wang, H. Zhang, A new Co-P nanocomposite with ultrahigh relaxivity for in vivo magnetic resonance imaging-guided tumor eradication by chemo/photothermal synergistic therapy, Small 14 (2018) 1702431.

[39] Z. Liang, N. Kong, C. Yang, W. Zhang, H. Zheng, H. Lin, R. Cao, Highly curved nanostructure-coated Co, N-doped carbon materials for oxygen electrocatalysis, Angew. Chem. Int. Ed. Engl. 60 (23) (2021) 12759–12764.
[40] M.P. Avanzi, O. Yeku, X. Li, D.P. Wijewarnasuriya, D.G. van Leeuwen, K. Cheung, H. Park, T.J. Purdon, A.F. Daniyan, M.H. Spitzer, R.J. Brentjens, Engineered tumor-targeted T cells mediate enhanced anti-tumor efficacy both directly and through activation of the endogenous immune system, Cell Rep. 23 (7) (2018) 2130–2141.
[41] E.W. Weber, M.V. Maus, C.L. Mackall, The emerging landscape of immune cell therapies, Cell 181 (1) (2020) 46–62.
[42] K.G. Mitchell, E.R. Parra, D.B. Nelson, J. Zhang, I.I. Wistuba, J. Fujimoto, J.A. Roth, M.B. Antonoff, E.M. Corsini, A.A. Vaporciyan, W.L. Hofstetter, R.J. Mehran, S.G. Swisher, D.C. Rice, B. Sepesi, G.L. Walsh, C. Behrens, N. Kalhor, A. Weissferdt, C. A. Moran, J.J. Lee, Tumor cellular proliferation is associated with enhanced immune checkpoint expression in stage I non-small cell lung cancer, J. Thorac. Cardiovasc. Surg. 158 (3) (2019) 911–919.e6.
[43] S.D. Blackburn, H. Shin, W.N. Haining, T. Zou, C.J. Workman, A. Polley, M.R. Betts, G.J. Freeman, D.A.A. Vignali, E.J. Wherry, Coregulation of CD8+ T cell exhaustion by multiple inhibitory receptors during chronic viral infection, Nat. Immunol. 10 (1) (2009) 29–37.
[44] H. Aghajanian, T. Kimura, J.G. Rurik, A.S. Hancock, M.S. Leibowitz, L.i. Li, J. Scholler, J. Monslow, A. Lo, W. Han, T. Wang, K. Bedi, M.P. Morley, R.A. Linares Saldana, N.A. Bolar, K. McDaid, C.-A. Assenmacher, C.L. Smith, D. Wirth, C.H. June, K.B. Margulies, R. Jain, E. Puré, S.M. Albelda, J.A. Epstein, Targeting cardiac fibrosis with engineered T cells, Nature 573 (7774) (2019) 430–433.
[45] M. Chang, Z. Hou, D. Jin, J. Zhou, M. Wang, M. Wang, M. Shu, B. Ding, C. Li, J. Lin, Colorectal tumor microenvironment-activated bio-decomposable and metabolizable $Cu_2O@CaCO_3$ nanocomposites for synergistic oncotherapy, Adv. Mater. 32 (43) (2020) e2004647.
[46] F. Gao, Y. Tang, W.-L. Liu, M.-Z. Zou, C. Huang, C.-J. Liu, X.-Z. Zhang, Intra/extracellular lactic acid exhaustion for synergistic metabolic therapy and immunotherapy of tumors, Adv. Mater. 31 (51) (2019) e1904639.
[47] W.-L. Liu, T. Liu, M.-Z. Zou, W.-Y. Yu, C.-X. Li, Z.-Y. He, M.-K. Zhang, M.-D. Liu, Z.-H. Li, J. Feng, X.-Z. Zhang, Aggressive man-made red blood cells for hypoxia-resistant photodynamic therapy, Adv. Mater. 30 (35) (2018) e1802006.